



**HAL**  
open science

# Enhancing Sustainable Construction Practices: Utilizing Heat-Treated Recycled Concrete Fines for Improving Slag-Based Geopolymer Materials

Amirouche Berkouche, Ahmed Abderraouf Belkadi, Abdelaziz Hasnaoui, Salima Aggoun, Abdelhak Khechai, Annelise Cousture, Tahar Tayebi, Tarek Chiker

## ► To cite this version:

Amirouche Berkouche, Ahmed Abderraouf Belkadi, Abdelaziz Hasnaoui, Salima Aggoun, Abdelhak Khechai, et al.. Enhancing Sustainable Construction Practices: Utilizing Heat-Treated Recycled Concrete Fines for Improving Slag-Based Geopolymer Materials. *Arabian Journal for Science and Engineering*, 2024, 10.1007/s13369-024-09477-6 . hal-04758457

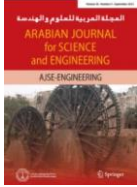
**HAL Id: hal-04758457**

**<https://hal.science/hal-04758457v1>**

Submitted on 29 Oct 2024

**HAL** is a multi-disciplinary open access archive for the deposit and dissemination of scientific research documents, whether they are published or not. The documents may come from teaching and research institutions in France or abroad, or from public or private research centers.

L'archive ouverte pluridisciplinaire **HAL**, est destinée au dépôt et à la diffusion de documents scientifiques de niveau recherche, publiés ou non, émanant des établissements d'enseignement et de recherche français ou étrangers, des laboratoires publics ou privés.



# Enhancing Sustainable Construction Practices: Utilizing Heat-Treated Recycled Concrete Fines for Improving Slag-Based Geopolymer Materials

Amirouche BERKOUCHE<sup>1</sup>, Ahmed Abderraouf BELKADI<sup>1</sup>, Abdelaziz HASNAOUI<sup>2</sup>, Salima AGGOUN<sup>3</sup>, Tarek CHIKER<sup>3,4</sup>, Abdelhak KHECHAI<sup>5</sup>, Annelise COUSTURE<sup>3</sup>, Tahar TAYEBI<sup>6\*</sup>

<sup>1</sup>Department of Civil Engineering, Bordj Bou Arreridj University, Algeria

<sup>2</sup>Department of Civil Engineering, University of Saad Dahlab Blida, Algeria.

<sup>3</sup>CY Cergy Paris Université, L2MGC, F-95000 Cergy, France

<sup>4</sup>ESITC-Paris, Arcueil, Paris, France

<sup>5</sup>Civil Engineering Research Laboratory, University of Biskra, Biskra, Algeria

<sup>6</sup>Mechanical Engineering Department, Faculty of Sciences and Technology, University Mohamed El Bachir El Ibrahimi of Bordj Bou Arreridj, El-Anasser, 34030, Algeria

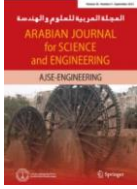
\*Correspondent author email: [Tahartayebi@gmail.com](mailto:Tahartayebi@gmail.com)

## Abstract

This study explores the untapped potential of utilizing heat-treated recycled fines (HT-RFs) from mortar as a sustainable and eco-friendly alternative for slag-based geopolymer materials in construction. The RFs undergo a novel heat treatment process at 650°C to significantly enhance their reactivity. Geopolymer mixtures incorporating both heat-treated and untreated RFs at various replacement ratios (0%, 10%, 20%, and 30%) are meticulously evaluated for their porosity, flexural strength, and compressive strength after 28 days of curing. The load-midspan displacement and failure behavior are analyzed using digital image correlation techniques. The microstructure of the mortar samples is comprehensively analyzed using state-of-the-art techniques including thermogravimetry, scanning electron microscopy, and X-ray diffraction. The results showed that incorporating 30% HT-RFs optimally enhanced the compressive and flexural strengths by 30.67% and 27.31% respectively, while substantially reducing the porosity by 16%, compared to the control geopolymer mixture. This study promotes sustainability in construction with eco-friendly materials by minimizing waste.

## Keywords

Recycled fine, thermal treatment, geopolymer, microstructure, image correlation



## 1. Introduction

In recent years, the construction industry has increasingly focused on sustainable and eco-friendly practices to reduce environmental impact and enhance resource efficiency. Various innovative approaches have been developed to achieve these goals, including the use of advanced materials and technologies. For instance, 3D printing technologies have emerged as a significant advancement, optimizing material usage and improving structural performance through precise and efficient construction methods [1], [2]. This technique not only minimizes waste but also allows for the creation of complex structures that would be challenging to achieve with traditional methods [3]. Additionally, sustainable practices such as the recycling of industrial by-products and the development of high-performance materials have contributed to reducing carbon footprints and promoting circular economies.

Among these sustainable materials, geopolymers have emerged as an innovative class of sustainable building materials gaining significant research attention and practical implementation [4]. Unlike ordinary Portland cement (OPC), geopolymers are synthesized utilizing locally available aluminosilicate sources such as fly ash, slag, clay minerals, silica sand, and recycled aggregates [5], [6]. The unique inorganic polymerization reaction induced by the alkaline activation transforms these raw materials into robust binders with comparable or superior properties to OPC-based binders [7]. Due to excellent compressive strength, durability, fire resistance, and relatively low carbon footprint, geopolymers are envisioned as next-generation binders aligned with the principles of sustainable construction [8], [9], [10].

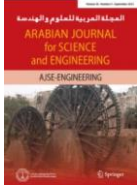
Nevertheless, a consistent supply of reactive silica and alumina precursors remains imperative for the widespread development of geopolymer technology [11]. In this regard, the valorization of construction and demolition waste (CDW) as potential aluminosilicate sources offers a promising solution. CDW refers to the heterogeneous waste streams generated from construction, renovation, and demolition activities encompassing concrete, bricks, tiles, metals, plastics, wood, and other materials [12], [13], [14], [15]. Two problems were solved at once when CDW was used to make geopolymers. First, they handle and dispose of large amounts of CDW internationally in an ecologically friendly manner [16]. Second, they enable the synthesis of alternative binders from the inherent reactivity of aluminosilicates in recycled aggregate and concrete fine fractions [17]. CDW-derived geopolymer binders reduce virgin raw material use and support the circular economy [18], [19].

Among the constituents of CDW, recovered fines and powders from crushed concrete, referred to as recycled fines (RFs), have gotten a lot of study interest. Concrete demolition waste forms the predominant category among global CDW volumes. While the coarse aggregates reclaimed from crushed concrete are reused in concrete production, the fine powder fraction is often landfilled. However, the cementitious components in the RFs present a unique opportunity to substitute conventional aluminosilicate precursors in geopolymer production. For instance, a recent study by Tan Jiawei et al. [20] synthesized geopolymers incorporating fine powders from mixed recycled aggregates (GMRA), achieving compressive strengths over 70 MPa. Another investigation by Saba et al. [21] analyzed the influence of partial substitution of RFs in geopolymer masonry mortars, finding improved interfacial bond strengths up to 20% RFs replacement levels. While reusing RFs as geopolymer precursors shows promise, it is vital to consider potential challenges impacting the performance based

on the composition and impurities in the recycled powders [22]. The reuse of RFs presents opportunities to utilize these materials as substitutes for natural resources in concrete production. However, the heterogeneous composition and impurities present in RFs can adversely impact their performance. To enhance the suitability of RFs as supplementary cementitious materials (SCM), researchers have explored various pre-treatment methods. These include techniques such as selective sieving and grinding to optimize the particle size distribution of RFs, magnetic separation to reduce iron impurities, and acid washing to remove deleterious compositions [23], [24], [25]. In addition, thermal treatment has been applied to alter the mineralogical and morphological properties of RFs beneficial for reactivity. The concept of restoring the hydration capacity of discarded cementitious substances by applying heat has been a subject of study in the pursuit of producing recycled binders. By raising the temperature, thermal activation can unlock the latent activity of mineral admixtures [26]. This concept originally stemmed from research on the recovery of strength in concrete following fire incidents [27], [28]. Numerous studies have provided confirmation that the recovery of strength is not solely attributed to the presence of leftover unhydrated cement particles, but also stems from the thermal activation occurring during the process. Previous research has consistently demonstrated a robust correlation between the thermal activation temperature (TAT) and the performance of RFs. A study by Shui and colleagues [29] found that optimal compressive and flexural strengths were attained when heat treatment was performed at 800 °C. However, strengths tended to decrease when the thermal treatment temperature exceeded 800 °C. On the other hand, Real et al. [30] found that the highest strength was attained when cement was dehydrated at 650 °C. These findings suggest that the optimal thermal treatment temperature for achieving maximum strength may vary depending on the specific materials and conditions used in the study. Additionally, research by Kalinowska-Wichrowska and coauthors [31] observed that increasing the TAT to 712°C boosted mortar compressive strength by 32%, and the mortar with 25% RFs heated to 650°C displayed water absorption akin to the control mortar which consisted of 100% cement. These findings indicate that higher TAT can significantly enhance the compressive strength of the mortar while maintaining comparable water absorption properties to traditional cement-based mortars. In their investigation, Serpell and Zunino [32] delved into the phase makeup, hydration reactivity, and mechanical performance of heat-treated recycled fines (HT-RFs) within the temperature range of approximately 700–900 °C. Notably, they found RFs processed at 740°C showed greater hydration heat release and produced pastes with higher compressive strength versus RFs treated at 860°C. This discrepancy was ascribed to the generation of a more reactive C<sub>2</sub>S polymorph variant under lower temperature conditions. The investigators ultimately deduced that the treatment temperature was the most important factor that affected both the heat of hydration and the compression strength.

In this scenario, digital image correlation (DIC) greatly increases our knowledge of material mechanical behavior and deformation. DIC gives accurate, full-field deformation and strain measurements that help us figure out how materials that have been treated react to loads. DIC is popular in research because to its cheap cost, efficacy, and ability to track displacements and stresses during experimental procedures [33]. The innovative optical approach DIC detects 2D and 3D displacement and strain without touch. The method compares digital photographs of a test location acquired at different load application stages. Pixels must be random, distinct, and high contrast for the system to work. The test area is generally prepared for DIC testing by can spraying a random dots pattern, although sometimes the natural surface's roughness is enough.

To date, there has been a lack of comprehensive research on the influence of HT-RFs on the behavior of slag-based geopolymers. Thus, the aim of this study is to tackle this knowledge gap by examining the



impact of RFs, treated at a high temperature of 650°C, on the characteristics of slag-based geopolymer composite mortars. The geopolymer mortars were formulated using granulated blast furnace slag (GBFS) and RFs as binders. The treated and untreated RFs were incorporated into the geopolymer mortar mixtures at replacement levels of 10%, 20%, and 30% by slag weight. The alkali activator in the mixtures consisted of sodium hydroxide (NaOH) and sodium silicate (Na<sub>2</sub>SiO<sub>3</sub>) solutions. After preparation, the mortar samples underwent 28 days of curing, followed by a comprehensive analysis using various methods. Thermogravimetric analysis (TGA), X-ray diffraction (XRD), mercury intrusion porosimetry (MIP), and scanning electron microscopy (SEM) were employed to characterize the materials. Additionally, load-displacement analysis and failure mode assessments, conducted through Digital Image Correlation (DIC), provided in-depth insights into the effect of RFs on the mechanical behavior and deformation patterns of the mortars. Compressive and flexural strength tests, along with the water-accessible porosity test, were also performed to comprehensively assess the mechanical and physical properties of the mortars. The findings from this study will offer valuable insights into the impact of HT-RFs on the geopolymerization process, contributing to the advancement of knowledge in this field.

## 2. Materials and methods

### 2.1. Raw materials

Recycled mortar fines (RFs) and granulated blast furnace slag (GBFS) were used as solid precursors in the test. GBFS sourced from a regional steel manufacturer (El-Hadjar complex, Annaba, Algeria) as spherical grains of 0/5 mm in particle size. RFs were generated from demolished mortar specimens. The rubble from the mortar samples was mechanically ground down and further pulverized in a ball mill. Next, a portion of the obtained RFs were subjected to heat treatment in a high temperature furnace. The temperature was ramped at 10 °C/minute from room temperature (20°C) up to 650°C. This temperature was maintained for 3 hours to ensure adequate activation of the HT-RFs [34]. The heat treatment process enhances the reactivity of the RFs by promoting the dehydroxylation of aluminosilicate phases and increasing the dissolution of silica (SiO<sub>2</sub>) and lime (CaO) [35]. This leads to the formation of more reactive species that improve the geopolymerization process. **Figure 1** exhibits the look of GBFS and HT-RFs post thermal activation processing.



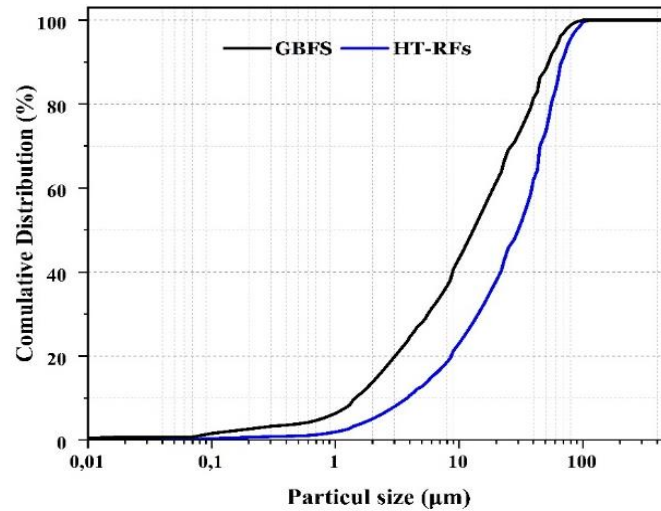
**Figure 1** Appearance of GBFS and HT-RFs

The Blaine-specific surface (BSS) and the density of GBFS and HT-RFs are presented in **Table 1**.

**Table 1** BSS and density of precursors

	Blaine specific surface (m <sup>2</sup> /Kg)	Density (g/cm <sup>3</sup> )
GBFS	525.0	2.40
RFs	451.3	2.315

The particle size distribution of HT-RFs and GBFS was determined using a particle size analyzer, the outcomes are illustrated in **Figure 2**. The particle size distribution of GBFS indicates a broader range of particle sizes, extending from 1.65 µm (at 10%) to 56.16 µm (at 90%). This suggests the presence of both fine and coarse particles in GBFS. On the other hand, the particle size distribution of the HT-RFs shows a narrower range, ranging from 4.01 µm (at 10%) to 72.07 µm (at 90%). The HT-RFs also exhibit a higher median particle size (32.03 µm) compared to GBFS (14.02 µm).



**Figure 2** Particle size distribution curves for GBFS and HT-RFs

**Table 2** shows the chemical compositions of GBFS and RFs, measured by X-Ray Fluorescence analysis. RFs have a significant amount of aluminosilicate minerals, with  $\text{SiO}_2$  and  $\text{Al}_2\text{O}_3$  constituting 42.7% and 2.91%, respectively, of its weight. This indicates that RFs can form an aluminosilicate gel system. On the other hand, slag contains much more calcium oxide than RFs, approximately 43.2%. In this paper, slag with a high content of calcium oxide was utilized to produce a calcium-rich aluminosilicate gel in the geopolymer matrix.

**Table 2** The chemical compounds of GBFS and RFs

%	CaO	SiO <sub>2</sub>	Al <sub>2</sub> O <sub>3</sub>	Fe <sub>2</sub> O <sub>3</sub>	K <sub>2</sub> O	Na <sub>2</sub> O	MgO	P <sub>2</sub> O <sub>5</sub>	TiO <sub>2</sub>	SO <sub>3</sub>	LOI
GBFS	43.2	41.1	7	2.8	0.32	0.6	4.7	-	-	0.25	0.03
RFs	39.2	47.6	3.25	3.43	0.62	0.605	2.29	0.34	0.206	1.56	0.8

## 2.2. Thermal analysis

Differential thermal analysis (DTA) was conducted to characterize the thermal behavior and phase changes of GGBFS, RFs, and HT-RFs (**Figure 3**). The DTA thermogram of RFs displayed an endothermic peak ranging between 450-500°C, indicative of the dehydroxylation of portlandite (calcium hydroxide -  $\text{Ca}(\text{OH})_2$ ) present in the mortar powder. As documented in earlier studies [36], [37], this endothermic effect is attributed to the thermal decomposition of portlandite to calcium oxide and water. In contrast, this distinct endothermic peak was absent in the DTA profile of HT-RFs. This corroborates that the portlandite phase in RFs undergoes dehydroxylation during heat treatment prior to DTA. Additionally, exothermic peaks were discerned between 700-800°C in the DTA plots of both RFs and HT-RFs. These exothermic reactions are potentially associated with the decarbonation of calcite ( $\text{CaCO}_3$ ) present in the powders, releasing calcium oxide and carbon dioxide at elevated temperatures, as hypothesized by Benosman et al. [38].

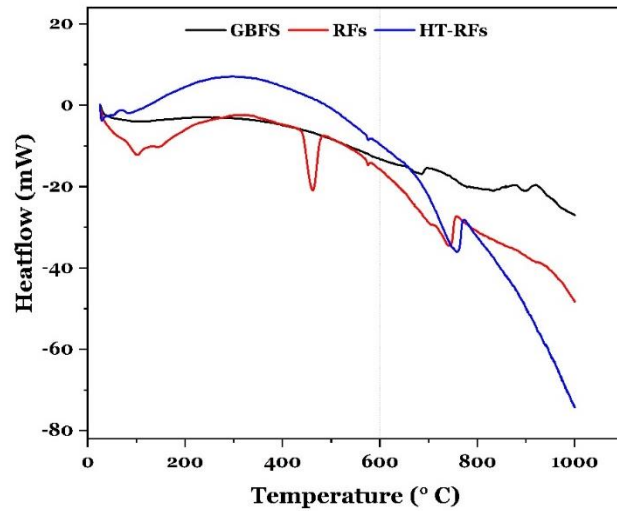


Figure 3 Curves of heat evolution rate of the precursors

### 2.3.XRD analysis

X-ray diffraction (XRD) analysis was conducted to characterize the phase compositions (**Figure 4**). GBFS exhibited an amorphous diffuse pattern without sharp crystalline peaks, indicating a predominantly vitreous structure with latent hydraulic reactivity. RFs showed a broad hump centered around  $29\text{-}30^\circ 2\theta$ , signifying abundant amorphous calcium silicate hydrate (C-S-H) gel phases. Additional lower intensity crystalline peaks corresponding to calcite and quartz were also detected. HT-RFs presented a distinctly different pattern with the disappearance of the broad hump. Enhanced crystallinity was evidenced by sharp well-defined peaks indexing to calcite, quartz, and calcium aluminate phases, suggesting decomposition of the original C-S-H gels.

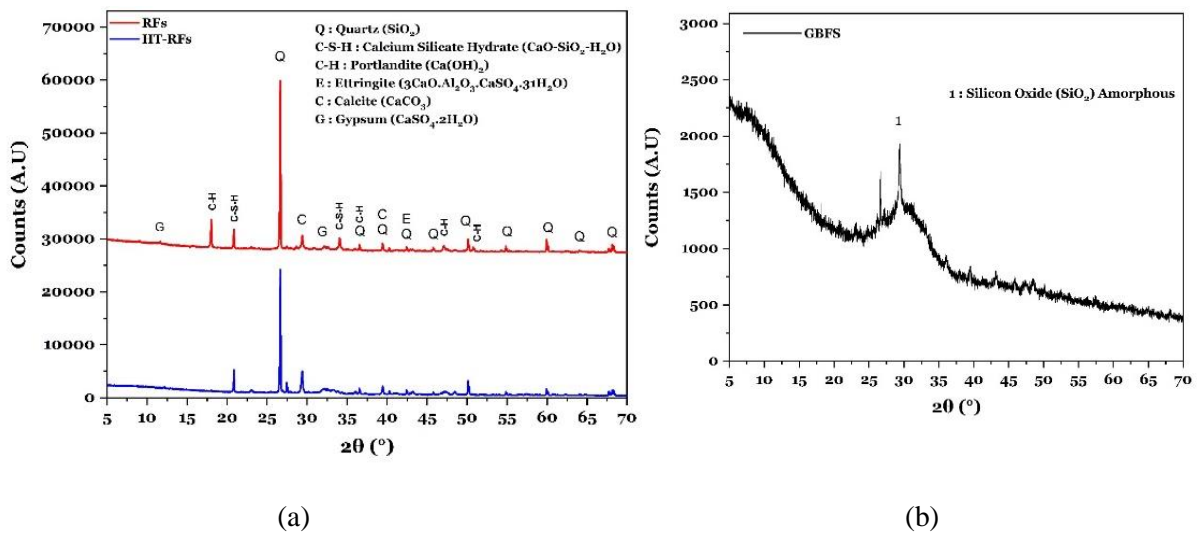


Figure 4 XRD results of the precursors (a) RFs and HT-RFs (b) GBFS

### 2.4.Samples preparation

The RFs and the HT-RFs were used to partly replace slag by mass in the mix proportion, as shown in **Table 3**. The blends were produced using a mortar mixer and cast into 40 mm x 40 mm x 160 mm prism



molds, with nine samples made per mixture. Per EN 196-1 [39], the specimens were cured for 28 days in a curing chamber at  $20 \pm 2^\circ\text{C}$  and a minimum 55% relative humidity.

**Table 3** Mix proportions of geopolymer mortar formulations.

Mixtures	MC	M10F	M20F	M30F	M10CF	M20CF	M30CF
GBFS (g)	504.36	454	403.5	353.05	454	403.5	353.05
RFs (g)	0	50.43	100.87	151.31	0	0	0
HT-RFs (g)	0	0	0	0	50.43	100.87	151.31
NaOH (g)	88.262	88.262	88.262	88.262	88.262	88.262	88.262
Na <sub>2</sub> SO <sub>4</sub> (g)	264.794	264.794	264.794	264.794	264.794	264.794	264.794
Sand (g)	1261	1261	1261	1261	1261	1261	1261

MC: Control mortar.

M10F, M20F and M30F: geopolymer mortars with 10 %, 20 % and 30 % replacements of RFs, respectively.

M10CF, M20CF and M30CF: geopolymer mortars with 10 %, 20 % and 30 % replacements HT-RFs, respectively.

## 2.5. Experimental Tests

### 2.5.1. Compressive and flexural strengths

Per EN 196-1 standard [39], an apparatus with maximum 3000 KN capacity was employed to carry out the compressive and flexural strength exams. The molds had dimensions of  $40 \times 40 \times 160$  mm. The average strength value of three samples from each mixture at 28 days after casting was taken as the ultimate flexural and compressive strength for each mixture.

### 2.5.2. Water-accessible porosity

The standard NF EN 18-459 [40] governs water-accessible porosity testing. This test measures concrete surface vacuum connection %. The test uses air-weighed and hydrostatic samples. The samples must be dried in a container at  $105^\circ\text{C}$  until the mass is consistent (less than 0.05% difference between 24-hour weighing).

### 2.5.3. Mercury intrusion porosimetry (MIP)

Mercury intrusion porosimetry (MIP) is a technique that reveals the pore structure of materials [41]. In this paper, MIP was conducted to evaluate the pore size distributions and porosities of the geopolymer paste samples containing 0%, 30% RFs, and 30% HT-RFs. The MIP analysis provided insights into the pore structure refinement induced by the thermal activation treatment compared to the untreated fines based on the incremental intrusion volume profiles.

### 2.5.4. Thermogravimetric analysis (TGA)

Thermogravimetric analysis (TGA) quantified phase weight losses by heating 20 mg samples from 30 to  $1000^\circ\text{C}$  at  $10^\circ\text{C}/\text{minute}$  under nitrogen.

### 2.5.5. Quantitative X-ray diffraction

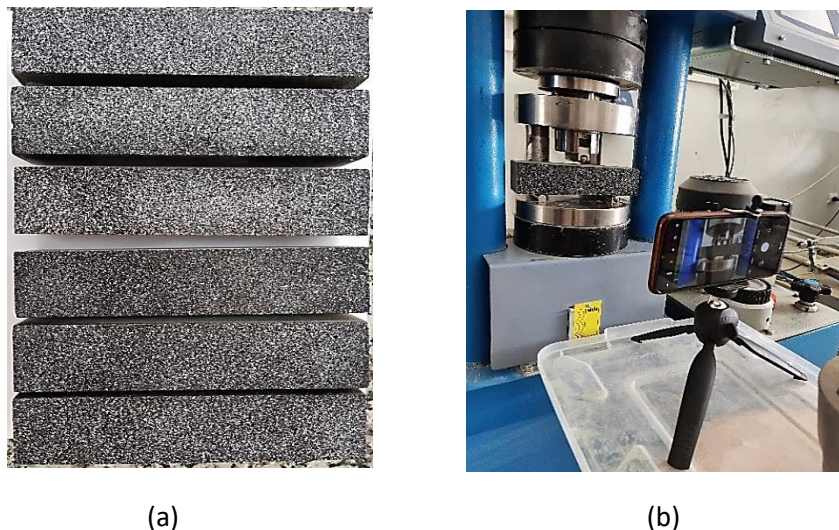
Quantitative X-ray diffraction analysis was conducted to determine and confirm the phase composition of the samples. The aim of QXRD analysis was to detect any detrimental phases that might have

originated from thermal cycles. And disclose the crystal structure and composition of the geopolymer mortar by analyzing the diffraction patterns of X-rays. XRD analysis can also furnish information about the crystallinity, lattice parameters, and preferred orientation of the phases.

#### 2.5.6. Digital image correlation analysis

In this work, the mechanical and failure behaviors of the manufactured mortars were analyzed using the robust digital image correlation (DIC) approach. Mortars' midspan load-displacement and failure behavior were analyzed using ZEISS's advanced GOM Correlate software (free version) [42], [43].

To prepare for DIC analysis, the surface of each mortar specimen was prepared with a speckle pattern. This pattern was created by spraying a random black-and-white speckle pattern onto the surface of the mortars, ensuring that the pattern had a high contrast necessary for accurate image correlation (**Figure 5-a**). The high-resolution images were then captured continuously during the loading process to record the deformation of the specimens. Utilizing the DIC technique, high-resolution images of the mortar surface were captured during the flexural strength test (**Figure 5-b**). The software proved instrumental in facilitating accurate measurements of displacement and strain distribution. By analyzing the strain fields and displacement maps obtained from DIC, we were able to determine the precise locations of crack initiation and monitor their growth under applied loads. This method allowed us to understand the failure mechanisms at a microstructural level, contributing to a comprehensive analysis of the mechanical performance of the geopolymer mortars. The implications of using DIC in this study are significant, as it enabled non-contact, full-field measurement of strain and displacement, thus providing a more detailed and accurate assessment of the mortars' behavior compared to traditional measurement techniques. This enhanced understanding is crucial for optimizing the mix design and improving the durability and performance of geopolymer-based construction materials.



**Figure 5** (a) The specimens with a speckle pattern viewed from the top (b) Image correlation device.

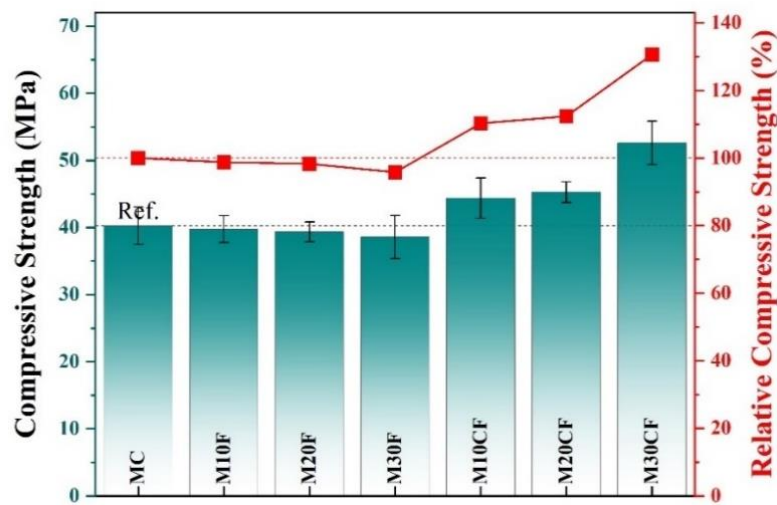
#### 2.5.7. Scanning electron microscopy

The samples' microstructure was assessed through scanning electron microscopy (SEM) without any coating. This analysis was performed using a Gemini 300 scanning electron microscope from ZEISS, which was outfitted with a Quantax 10 X-ray microanalysis detector by Bruker. The observations were conducted under variable pressure conditions, either at 75 or 150 Pa, with a specific working distance of XX mm and an acceleration voltage of 15 kV.

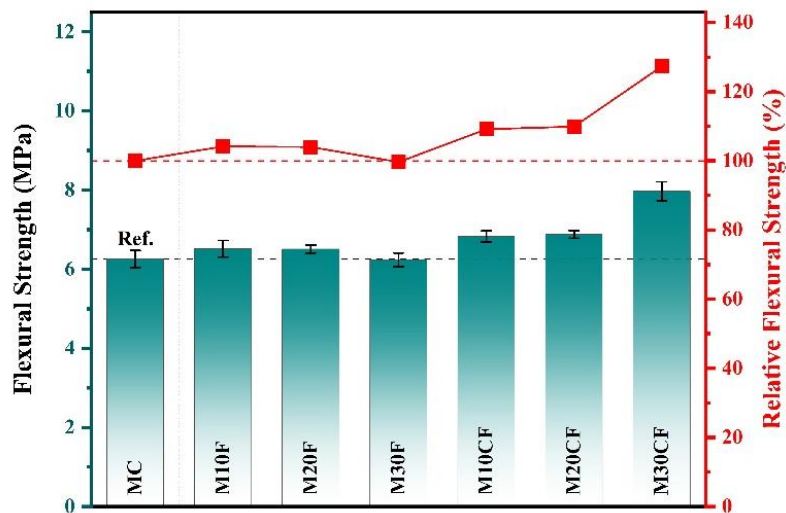
### 3. Results and discussion

#### 3.1. Compressive and flexural strengths

To assess the mechanical properties of geopolymer mortars, compressive and flexural strength were evaluated at 28 days, as shown in **Figure 6** and **Figure 7**.



**Figure 6** Compressive strength results across geopolymer mortars



**Figure 7** Flexural strength values of geopolymer mortars

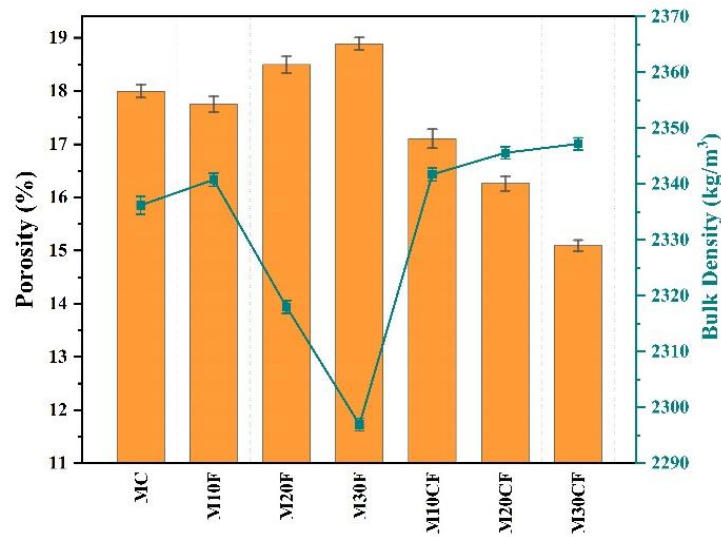
The incorporation of RFs has an influence on the mechanical strength of the newly made mortars. For instance, the compressive strength (CS) values of the mixtures containing RFs (M10F, M20F, and M30F) were 39.78 MPa, 39.36 MPa, and 38.59 MPa, respectively, while MC achieved a CS of 40.27 MPa. This resulted in a decrease in CS values for M10F, M20F, and M30F by 1.22%, 2.26%, and 4.17%,

respectively, compared to MC. The rate of reduce in strength increased as the RFs replacement ratio increased, primarily due to the decreased CaO content from the presence of slag in the geopolymer matrix. This, in turn, accelerated the geopolymerization process and the formation of the calcium aluminosilicate hydrates (C-A-S-H) gel [44]. Additionally, slag contributed to filling up pores and voids, enhancing the strength of the matrix [45]. Consequently, replacing slag with RFs in geopolymer mortars led to a reduction in CS results. However, when considering the flexural strength (FS) (**Figure 7**), mixtures containing RFs (M10F, M20F, and M30F) exhibited FS values of 6.52 MPa, 6.51 MPa, and 6.23 MPa, respectively, compared to the FS of the control mortar at 6.26 MPa. These findings indicate that incorporating RFs as a partial replacement for slag did not have a significant impact on the FS of the resulting mortars. In fact, FS values of mortars containing RFs were comparable to those of the control mortar, with the highest value recorded for M20F.

On the other hand, a dramatic increase in in both CS and FS were observed in all mixtures containing HT- RFs (M10CF, M20CF, and M30CF). For instance, CS values were 44.40 MPa, 45.27 MPa, and 52.62 MPa, respectively, representing an increase of up to 10.26%, 12.41%, and 30.67% compared to MC. Similarly, the FS exhibited enhancements upon incorporating HT-RFs at substitution rates of 10%, 20%, and 30%, with values of 6.83 MPa, 6.88 MPa, and 7.97 MPa, respectively. The highest FS value was recorded for M30CF, indicating a 27.31% increase compared to MC. Several factors can explain the observed improvements in mechanical strength. Firstly, the thermal treatment process eliminated organic matter from the RFs, resulting in a stronger geopolymer structure. Organic matter can introduce voids or weak points that negatively affect the mechanical properties and porosity of the geopolymer structure [46]. Additionally, the thermal treatment process improved the physical properties of the HT-RFs. The high temperatures during the treatment caused the formation of new minerals and the breakdown of aluminosilicate phases [47]. Moreover, this observation can also be attributed to the presence of amorphous phases and dicalcium silicate ( $C_2S$ ) in the HT-RFs that underwent calcination at  $650^{\circ}C$ . The amorphous phases refer to non-crystalline structures formed during the calcination process. These amorphous phases can contribute to the reactivity and bonding potential of the material. Furthermore, according to Sanchez et al. [48], the presence of  $C_2S$  in an alkali medium can have a positive effect on the mechanical strength of the resulting material.  $C_2S$ , when exposed to alkali solutions, undergoes reactions that lead to the formation of additional reaction products, including calcium silicate hydrate (C-S-H) gel. Therefore, the combination of amorphous phases and the presence of  $C_2S$  in the calcined powder can potentially explain the observed improvement in mechanical strength. These factors contribute to the reactivity and formation of stable binding phases, ultimately resulting in a geopolymer with enhanced mechanical performance. Besides, according to Mirghiasi et al. [49], CaO can be produced by direct thermal-decomposition of  $Ca(OH)_2$ , at  $650^{\circ}C$ , the CaO formed can facilitate the development of calcium-rich phases within the geopolymer matrix. These phases, such as C-A-S-H, serve as nucleation sites for the growth of additional binding materials [50]. Research by Zhang et al. [51] shows that RFs are rich in minerals like  $Ca(OH)_2$ , C-S-H, and clay. Calcination at the proper temperatures causes the breakdown of these minerals, resulting in phases that are amenable to the hydration process. By promoting the formation of these calcium-rich phases, the voids in the geopolymer structure can be filled, thereby strengthening the material, and resulting in improved mechanical strength. The newly formed CaO also undergoes a pozzolanic reaction with alkaline activators, such as sodium hydroxide, leading to the formation of C-S-H gel [52]. This is consistent with the DT/TG results in (section 3.4) showing thermal decomposition of calcium hydroxide and carbonate in HT-RFs between  $400-800^{\circ}C$  to produce reactive CaO. The reaction of this nascent CaO with NaOH thus causes additional C-S-H formation, confirming the synergistic effects of heat treatment and alkali-activation in enhancing the reactivity of RFs.

### 3.2. Water-accessible porosity

Results for all mortar samples' water-accessible porosity and density are shown in **Figure 8**.



**Figure 8** Water absorption results of obtained mortars

The water-accessible porosity test results indicate that incorporation of RFs led to higher porosity values ranging from 17.75% for M10F up to 18.89% for M30F, compared to 17.99% for MC. The increase in porosity correlates to the progressively higher RFs content, implying that RFs introduce additional voids and imperfections into the microstructure. This aligns with the poor interfacial bonding and lack of particle packing efficiency expected with hydrophobic unincorporated fines, this interpretation is supported by Gao Q et al. [53] which have investigated the capillary absorption behavior of recycled aggregate concrete with deferent replacement percentages of RFs. In addition, when RFs are used to replace slag in the geopolymer matrix, they reduce the quantity of aluminosilicates that can react with the alkaline activators and form new geopolymer products that are important for filling the pores and cracks in the geopolymer matrix and making it denser and more impermeable [45].

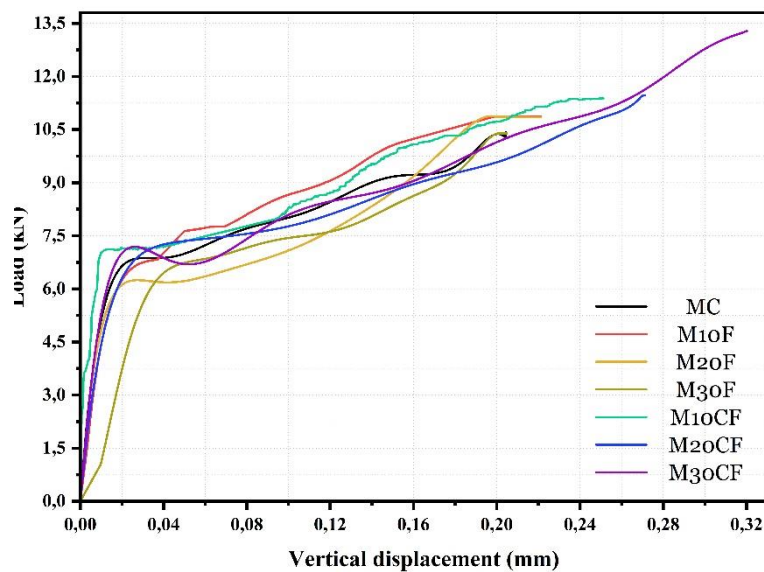
In contrast, the mortars containing HT-RFs showed decreased porosities reducing from 17.10% for M10CF down to 15.09% for M30CF. The porosity refinement signifies that the heat treatment of fines improves incorporation into the binder matrix, enabling denser microstructures. The enhanced hydration reactivity and particle packing efficiency of the treated fines allows for reduced voids. As discussed under the title of mechanical strength, the thermal treatment removes the organic matter that creates voids for water to penetrate the matrix. Also, the presence of amorphous phases of silicate contributes to the formation of supplementary C-A-S-H gel in the medium, which is known to be compact and dense [54]. This gel can fill the pores and make them finer, leading to reducing the porosity of the mortars. Furthermore, the heat treatment process at 650°C results in the formation of CaO within HT-RFs. This CaO can react with aluminosilicates present in the geopolymer system to form C-A-S-H gel. The formation of C-A-S-H gel has been reported to contribute to the filling of pores and the creation of a denser structure in geopolymer materials [55]. The densification of the structure through the formation of C-A-S-H gel can significantly enhance the resistance to water absorption in the mixtures.

Regarding density, MC showed the highest value of 2336 kg/m<sup>3</sup>, while densities ranged from 2296-2340 kg/m<sup>3</sup> for mortars containing RFs and 2325-2347 kg/m<sup>3</sup> for mortars with HT-RFs. The slight density reductions correlate to the increased porosities from the unincorporated recycled fines particles.

### 3.3. Digital image correlation analysis

#### 3.3.1. Load-midspan displacement

**Figure 9** depicts the load-displacement curve of flexural force-applied specimens. Every sample showed evidence of strain relaxation, and a straight slope line could be seen from the onset of strain to the development of micro-cracks. As the applied stress was initially successfully handled by the uncracked material, the specimen's load-displacement curve showed an initial linear elastic area. According to Xie et al. [56], the initial stage of loading exhibits a linear relationship between load and deflection, which is consistent with the anticipated behavior as the fly ash-based GPC experiences linear elastic deformation. The outcomes from DIC analysis illustrated in **Table 4** reveal that MC exhibited a peak load of 10.43 kN, brittle fracture occurred as the flexural strength was exceeded. The rapid loss of load carrying capacity coupled with the very low displacement at failure of 0.204 mm signifies that MC experienced a highly brittle fracture with minimal plastic deformation prior to failure.



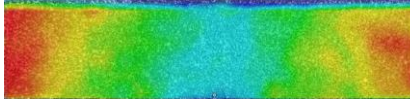
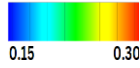
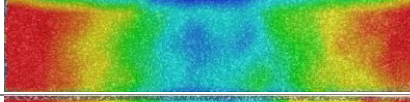

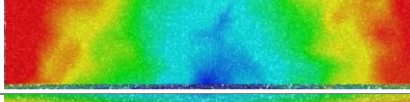

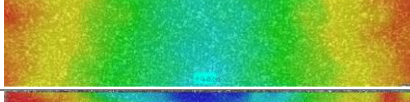

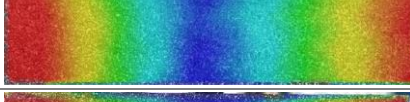

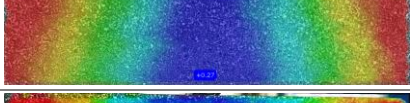
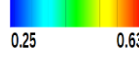
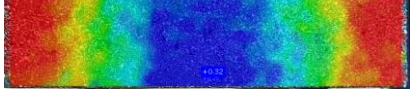

**Figure 9** Load-displacement curves obtained from DIC.

In comparison, M10F and M20F displayed marginal improvements in both peak load (up to 10.87 kN) and displacement at failure (up to 0.22 mm) relative to the control MC mortar. The modest enhancements in ductility suggest that the incorporation of untreated fines was able to provide a limited contribution in terms of deformation capacity and energy absorption prior to failure. This may be attributed to the untreated fines acting as microfillers that increase fracture surface area and provide minor crack arresting effects. However, M30F showed a reduction in displacement at failure back to 0.205 mm along with a lowered peak load of 10.39 kN compared to M20F. This implies that beyond a threshold of around 20%, the higher porosity and poor cohesion of excessive untreated fines began to have detrimental effects, overriding any minor benefits. The impaired performance signifies poor interfacial adhesion between RFs and the matrix at higher contents, resulting in inadequate stress transfer.

In contrast, the HT-RFs replacement (M10CF, M20CF, M30CF) led to more pronounced improvements in peak load and deformation capacity. The peak loads increased consistently from 11.38 kN up to 13.28 kN while the displacements at failure improved significantly from 0.251 mm up to 0.32 mm relative to the control. This behavior indicates that the thermal treatment enhanced the ductility and fracture energy absorption of the mortars by facilitating hydration reactions and pozzolanic activity from RFs. The refined microfillers were able to provide internal reinforcement through crack bridging and obstruction effects. In addition, according to Wu et al. [35], the activated fines improved interfacial transition zones

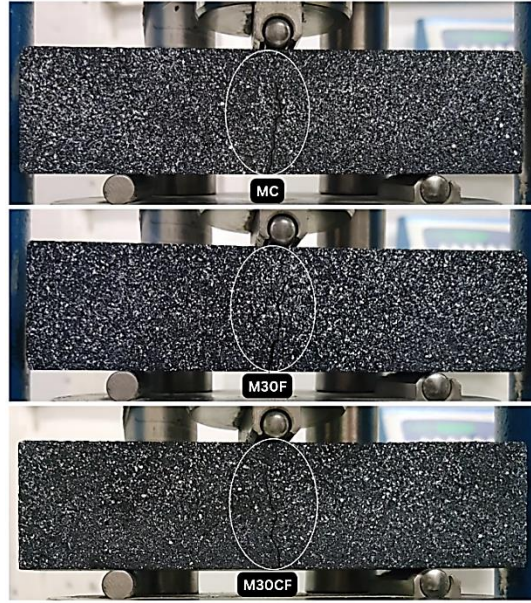
between the particles and matrix, enabling more efficient stress transfer. These synergistic mechanisms resulted in the shift from brittle behavior in the control mortar to pseudo-ductile behavior aided by the incorporation of treated RFs.

**Table 4** Vertical displacement results obtained by DIC at ultimate loads.

Specimen	Measurement point	Graphical vertical displacement	Legend	Load (kN)	dy (mm)
MC	Mid-span			10.43	0.204
M10F				10.87	0.22
M20F				10.85	0.221
M30F				10.39	0.205
M10CF				11.38	0.251
M20CF				11.46	0.271
M30CF				13.28	0.32

### 3.3.2. Failure behavior

**Figure 10** illustrates the failure modes of three key mixtures: MC, M30F, and M30CF. MC shows a typical crack pattern with moderate deformation. M30F, however, exhibits multiple cracks and widespread deformation, indicating a lower resistance to fracture. This suggests that while M30F may possess good initial strength, its overall durability and long-term performance could be compromised due to the extensive cracking under stress. In contrast, M30CF demonstrates localized deformation with fewer cracks, pointing to a higher rigidity and enhanced performance under load [57]. Additionally, the localized deformation can be attributed to the improvement of modulus of elasticity, indicating that M30CF not only resists cracking better but also retains its structural integrity under stress [58]. The enhanced modulus of elasticity reflects the mixture's ability to deform less under the same load compared to MC and M30F, further supporting the observation that M30CF has superior mechanical properties.



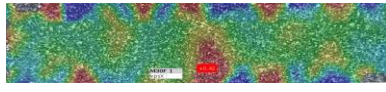
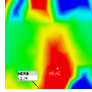
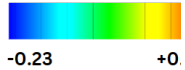
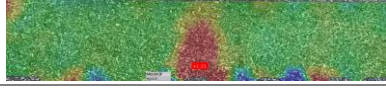
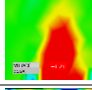
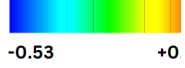
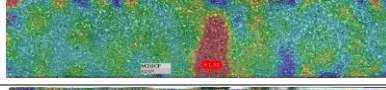
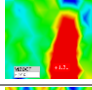
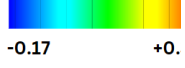

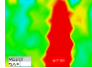
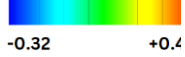
**Figure 10** Crack propagation at failure for key mixtures

For a more detailed analysis, DIC provides a comprehensive view of the strain distribution across the samples. The image correlation findings (**Table 5**) reveal that RFs and HT-RFs may affect mortar failure behavior. Due of its poor flexural strength, the MC specimen showed many microcracks equally distributed under loading. However, the very low mid-span crack width of 1.64 mm indicates highly localized and severe damage for MC, characteristic of extremely brittle failure with low ductility. Crack widths increased 3.48-3.88 mm in M10F and M20F compared to MC. Wider RFs allow for more deformation and energy absorption before failure, lowering brittleness. However, the many fractures indicate structural integrity issues and stress concentrations from poor matrix-porous RF compatibility. An ideal 10-20% RF content matched energy dissipation and fracture resistance. Beyond this level, flaws from RF agglomerations induced a reversion to more localized brittle failure as shown in M30F, which demonstrated a decreased fracture width of 1.68 mm. Crack widths rose from 4.84 mm to 10.76 mm in mortars with 10-30% HT-RFs. Widening fractures indicate brittle to ductile failure, with heat-treated RFs giving mortars more ductility and toughness. Dispersed microcracks in M20CF indicate successful stress distributions from engineered RFs. Past the ideal 20-30% HT-RFs range, stress concentrations exceeded improvements, causing localization.

**Table 5** Failure mode and crack width results obtained from DIC.

Specimen	Measurement point	Graphical crack	3D view	Legend	Crack width (%)	Crack width (mm)
MC	Mid-span				0.41	1.64
M10F					0.87	3.48
M20F					0.97	3.88



<b>M30F</b>				0.42	1.68
<b>M10CF</b>				1.21	4.84
<b>M20CF</b>				1.31	5.24
<b>M30CF</b>				2.69	10.76

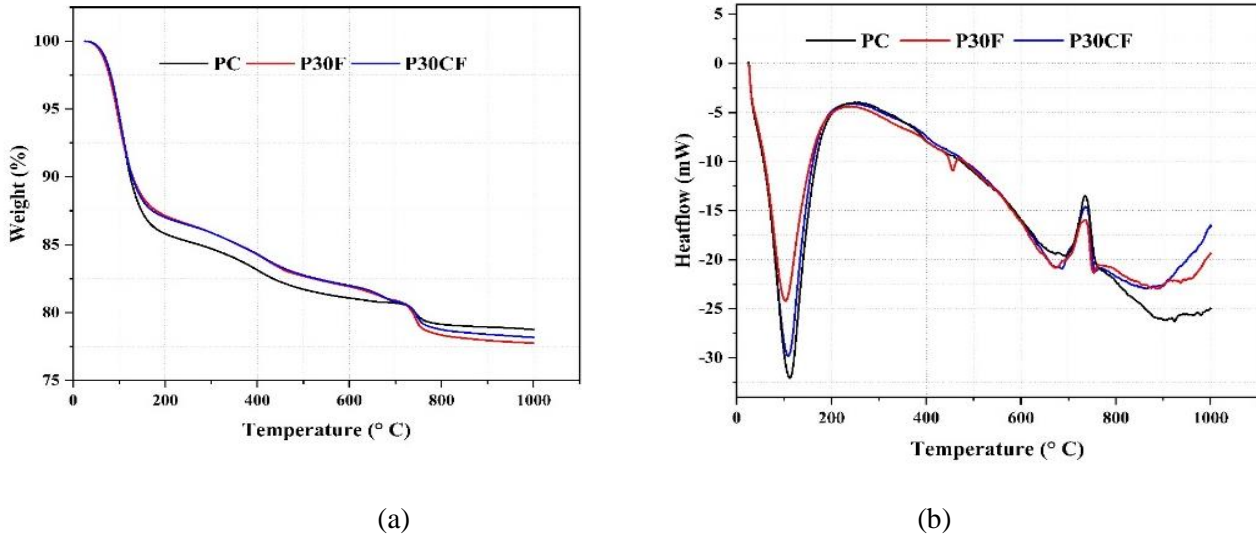
Crack width indicates damage severity. Brittleness increases with decreased crack width. The results obtained from DIC found that adding HT-RFs increases fracture width because thermal treatment increases RFs' reactivity and hydration potential. The formation of more C-S-H and C-A-S-H gels reinforces the microstructure and increases energy dissipation by microcracking. Fillers like finely distributed activated particles prevent fracture growth. As reported by Sarker et al. [59], the improved crack resistance is attributed to the improved bonding between particles and the formation of a more cohesive and interconnected microstructure. The greater crack width at midspan indicates ductile pseudo-strain hardening rather than rapid brittle fracture failure. Heat treatment refines particle packing and transition zones, allowing fractures to spread through the matrix.

### 3.4. Thermogravimetric analysis (TGA)

**Figures 11** show the DTA/TGA results for control paste (PC), paste with 30% RFs replacement (P30F), and paste with 30% HT-RFs replacement (P30CF). During the heating process up to 100 °C, all pastes displayed a distinct and abrupt decrease in mass, as indicated by the sharp drop on the TG curve. This phenomenon can be attributed to the loss of adsorbed water present within the paste samples [60]. Adsorbed water refers to the moisture that is physically bound to the surface of the materials.

All DTA curves displayed an endothermic peak from 50 to 150°C, linked to ATG mass losses attributed to C-S-H and silica gel dehydration [36], [61], [62]. Among the pastes, PC exhibited the highest endothermic peak within this temperature range, indicating a higher content of C-S-H compared to the other pastes. Additionally, the P30CF showed a relatively higher endothermic peak compared to P30F. This can be explained by the presence of amorphous phases resulting from the heat treatment process. Furthermore, the P30F exhibited an additional endothermic peak between 450°C and 500°C. This peak can be attributed to the dehydroxylation of calcium hydroxide  $\text{Ca}(\text{OH})_2$  present in the paste, which decomposed during the TG test as described by Argiz et al. [37], Benosman et al. [38], and Hidalgo et al. [63]. In contrast, P30CF did not show this peak as its portlandite had already decomposed during the heat treatment process.

Additionally, exothermic peaks were observed in all pastes between 700°C and 800°C, indicating the occurrence of chemical reactions at elevated temperatures. These peaks can be linked to the decarbonation of calcite ( $\text{CaCO}_3$ ), as suggested by previous investigations [38], [64]. Calcite is commonly present in cementitious materials and its decomposition releases carbon dioxide ( $\text{CO}_2$ ) and generates heat. The exothermic peaks observed in the TGA test within the specified temperature range can be attributed, at least in part, to the decarbonation of calcite.



**Figure 11** TG/DT analysis results of obtained pastes (a) weight loss (b) Heatflow

### 3.5.XRD analysis

The XRD patterns of the geopolymer pastes are depicted in **Figure 12**. The XRD pattern of PC exhibits a similarly broad hump as GGBFS powder (Section 2.3). This hump spans  $\sim 15\text{-}35^\circ 2\theta$ , indicating the presence of the aluminosilicate geopolymer gel phase. However, the intensity of this amorphous hump is distinctly greater in PC to GBFS precursor. This verifies the enhanced dissolution of the reactive vitreous slag components and their condensation into the final geopolymer gel network upon alkali activation. The escalated intensity reflects an increase in the amount of geopolymer gel binder phase formed as a result of polycondensation of the dissolved aluminosilicate species released from the amorphous glassy slag during the alkali activation process [65]. Moreover, the breadth and general profile of the hump remains analogous to GBFS, suggesting that the short-range disordered nature of the original glassy structure is retained while mainly increasing the abundance of the gel product [66]. The absence of any sharp crystalline peaks confirms the essentially amorphous network structure of the hardened geopolymer gel binder synthesized through alkali-activation of the vitreous GBFS precursor. The XRD pattern of P30F exhibits the broad hump spanning  $15\text{-}35^\circ 2\theta$  arising from the amorphous aluminosilicate geopolymer gel phase formed upon alkali-activation of GBFS. The presence of this distinct hump verifies that partial geopolymerization has occurred through dissolution and recondensation of the reactive slag components. However, the hump intensity and breadth are markedly reduced compared to P30CF sample. This diminishment indicates that the abundant C-S-H gels available in the RFs have only engaged in limited and incomplete geopolymerization. A large proportion of C-S-H phases likely persist as discrete unreacted components within the microstructure without integrating into the final cross-linked geopolymer gel network. Additional low intensity crystalline peaks from calcite and quartz also emerge, signifying partial cement hydration reactions of residual anhydrous cement particles in the untreated powder [67]. However, the crystalline phase amounts remain low. The incomplete dissolution and participation of C-S-H gels from the RFs is further verified through thermogravimetric analysis, which quantified a lower C-S-H content compared to the heat-treated variant. This limited C-S-H reaction hinders extensive geopolymer formation and interconnectivity, contributing to the inferior mechanical properties exhibited by this sample [68].

In contrast, P30CF displays a substantially more intense amorphous hump versus P30F sample. The greater intensity conclusively verifies that the reactive siliceous components in the HT-RFs have extensively dissolved and engaged in polycondensation reactions to form abundant aluminosilicate geopolymer gel. Moreover, much sharper crystalline peaks from calcite, quartz, portlandite and ettringite are clear. The intensity escalation confirms that the thermal treatment has enhanced the hydraulic reactivity of the recycled fines to undergo supplementary hydration and pozzolanic reactions upon activation. The efficacy of the thermal treatment in elevating the reactivity of the fines is further validated through the greater C-S-H gel content quantified by TGA (Section 3.4). This results in the superior mechanical properties exhibited by this sample, aligning with the compressive and flexural strength improvements.

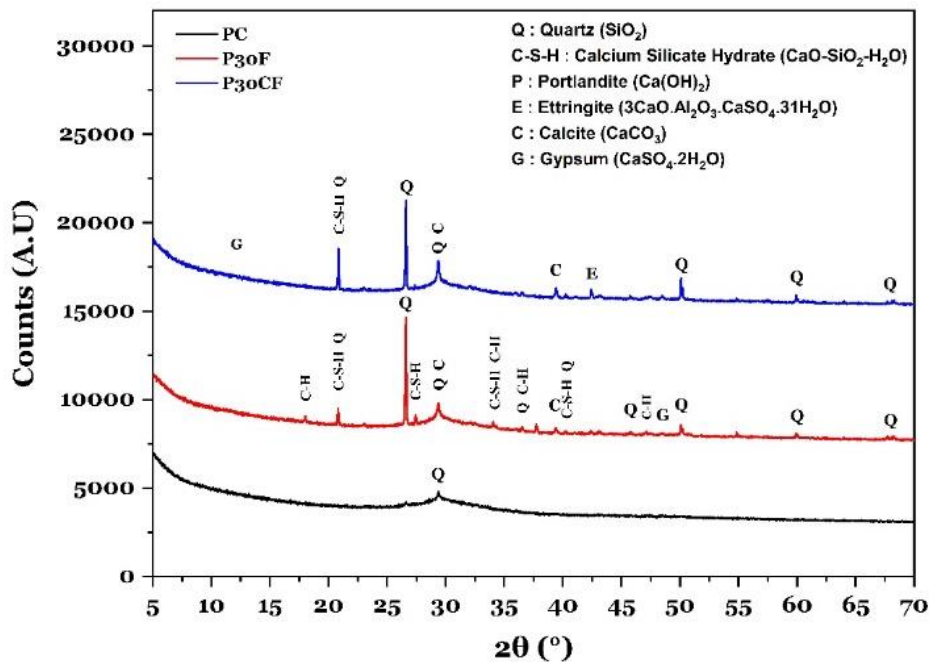
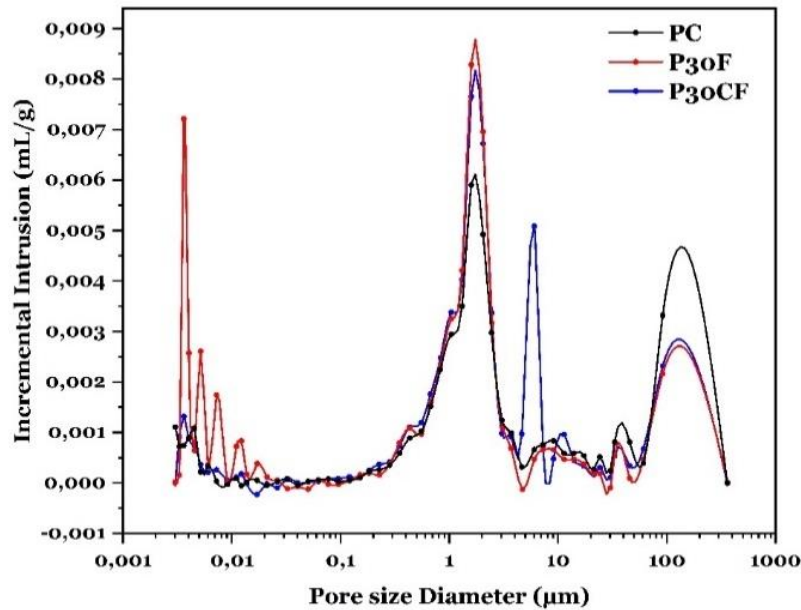


Figure 12 XRD results of obtained pastes.

### 3.6.Pore structure analysis using Mercury Intrusion Porosimetry

The findings from the pore structure analysis, conducted using Mercury Intrusion Porosimetry (MIP), are presented in **Figure 13**.



**Figure 13** Pore structure analysis results of pastes based on MIP.

The control paste exhibited a sharp predominant micropore peak at 0.01  $\mu\text{m}$  pore diameter, representing interparticle voids between geopolymer gel nanoparticles as the primary binding phase. The 0.01  $\mu\text{m}$  peak center indicated consistent gel aggregate sizes formed through homogenous polycondensation of the reactive slag source [69]. The high 0.01  $\mu\text{m}$  peak intensity verified abundant development of these mesopores within the condensed gel network. The incremental intrusion plateau from 0.02-0.5  $\mu\text{m}$  range implied optimized packing density and consolidation. The absence of any noticeable secondary capillary pore peak confirmed minimization of larger flaws between packed gel clusters [70]. The drastic volume decline above 10  $\mu\text{m}$  signified substantial densification of residual pores, with negligible intrusion detected up to the maximum diameter of 359.239  $\mu\text{m}$ .

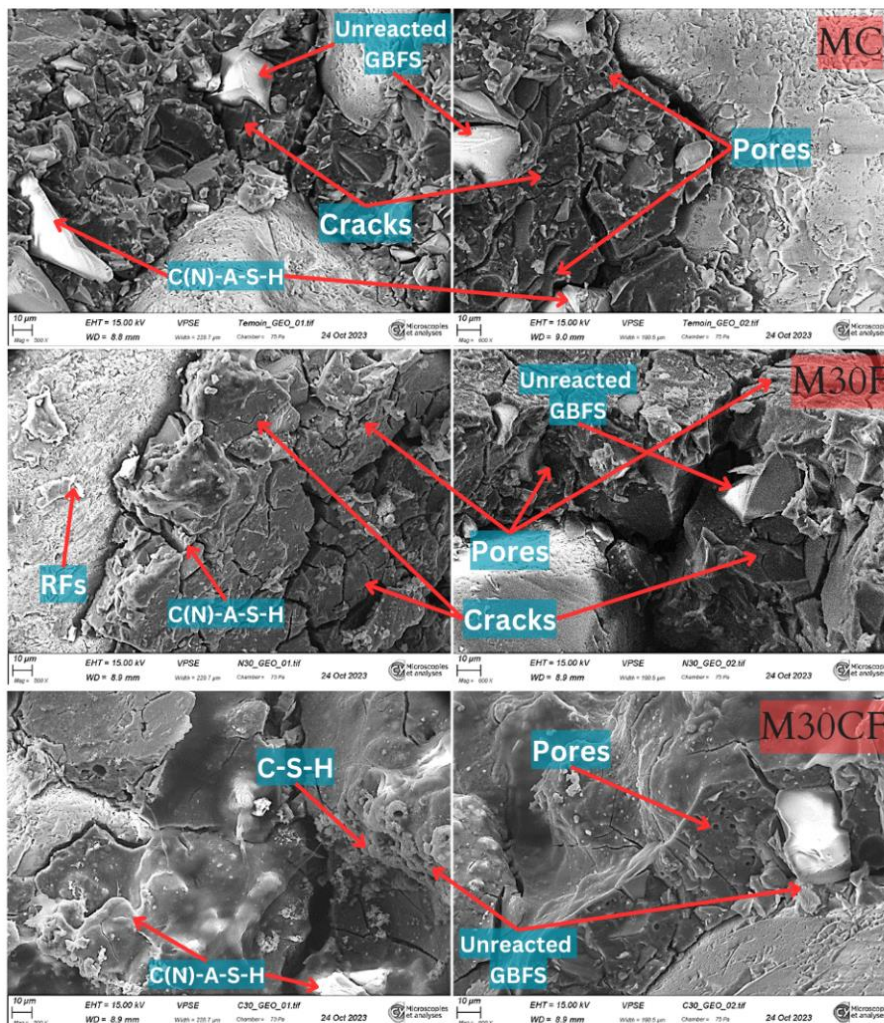
In contrast, P30F exhibits a broader, less defined mesopore peak centered at 0.02  $\mu\text{m}$  spanning 0.01-0.05  $\mu\text{m}$ , indicating less uniform inter-particulate voids with inconsistent gel aggregate sizes around 0.02  $\mu\text{m}$ . The higher peak intensity of 0.0076 mL/g suggests increased abundance of these mesopores due to discontinued consolidation. The elevated incremental intrusion from 0.05-0.5  $\mu\text{m}$  range implies additional flaws between packed gel clusters preventing adequate densification. The secondary peak from 1-10  $\mu\text{m}$  signifies uncontrolled large capillary pores likely from discrete unreacted C-S-H phases. The steady incremental volume up to the maximum diameter of 364.281  $\mu\text{m}$  verifies pore continuity rather than an optimized condensed nanostructure. Overall, the profile indicates significant defects in the nanostructure densification and attainment of uniform nanoporosity in P30F. This defective microstructure induces inferior mechanical performance compared to PC.

In contrast to P30F, P30CF displayed a sharp 0.01  $\mu\text{m}$  mesopore peak position similar to PC. This comparable peak location indicates equivalent nanoscale gel aggregation and pore structure homogenization was achieved in the sample with HT-RFs. The analogous 0.01  $\mu\text{m}$  peak volume and intensity verifies that tailoring the RFs through heat-treatment facilitated their integration into a densified binder network with uniform mesoporosity matching the control paste. This consolidation and flaw minimization provides superior load-bearing capacity. Additionally, the minimal incremental intrusion volume in the 0.02-10  $\mu\text{m}$  range approached the negligible levels seen in PC. This pore refinement confirms that the thermal activation induced densification across length scales, preventing formation of micro-cracks or passages for strength-degrading agents. The equivalent maximum pore

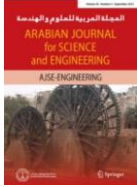
diameter of 359.580  $\mu\text{m}$  further substantiates that heat-treatment enabled substantial microstructure optimization and consolidation. This replicates the mechanical performance enhancements observed in PC. The MIP results validate that tailored thermal activation of RFs facilitated their seamless incorporation into the geopolymer nanostructure, inducing synergistic densification and strength improvements matching the control paste.

### 3.7. Scanning electron microscopy analysis

SEM pictures of MC, M30F, and M30CF are shown in **Figure 14**. In MC, the SEM image reveals the presence of unreacted GBFS particles embedded within the aluminosilicate matrix. This is confirmed through the EDX results (**Figure 15**, spectra 1) showing the elemental composition of magnesium, calcium, and aluminum rich regions corresponding to residual GBFS. The incomplete slag reaction indicates that not all the calcium silicate phases have participated in the alkali activation process. Meanwhile, EDX spectra (2) displays high silicon, aluminum, and sodium content, which provides evidence of C(N)-A-S-H gel formation suggesting the geopolymerization of the aluminosilicates has occurred to some extent. However, microcracks are observed surrounding the unreacted GBFS particles. These cracks likely arise from shrinkage stresses and poor interfacial transition zones between the slag particles and the geopolymer binder matrix.



**Figure 14** SEM pictures of geopolymer mortars



For M30F, the C(N)-A-S-H gel is again detected through the high silicon, aluminum, and sodium contents in EDX spectra (3). This implies the alkali activation process has taken place despite the RF incorporation. Meanwhile, the EDX spectra (4) shows the presence of unreacted RF particles within the microstructure, characterized by high silicon content. The poor compatibility between RFs and the geopolymer matrix leads to a more heterogeneous microstructure compared to MC. Additionally, more extensive cracking and numerous pores are observed in the M30F microstructure, which can be attributed to the porosity and lack of cohesion of the RFs particles with the surrounding matrix. The pores and poor particle packing of the untreated RFs contribute to the increased microcracking under loading.

Finally, in M30CF, the C(N)-A-S-H gel formation is again evidenced by EDX spectra (5). Unreacted GBFS particles are still detectable, as indicated by the magnesium and calcium rich regions in EDX spectra (6) suggesting slag has not fully reacted. Notably, EDX spectra (7) displays elevated calcium and silicon content, providing evidence of additional C-S-H gel formation resulting from the enhanced hydraulic reactivity imparted through RF heat-treatment. This supplementary C-S-H gel leads to a densified microstructure with improved particle packing and interfacial bonding between the refined RFs and the geopolymer matrix. The SEM image of M30CF reveals a very dense microstructure compared to MC and M30F, resulting from the enhanced packing density and hydraulic phase additions from the thermally activated RFs. Thus, the SEM/EDX analysis confirms that thermal treatment of RFs enables incorporation of additional hydraulic phases leading to enhanced mechanical performance, while untreated RFs results in poor microstructural cohesion.

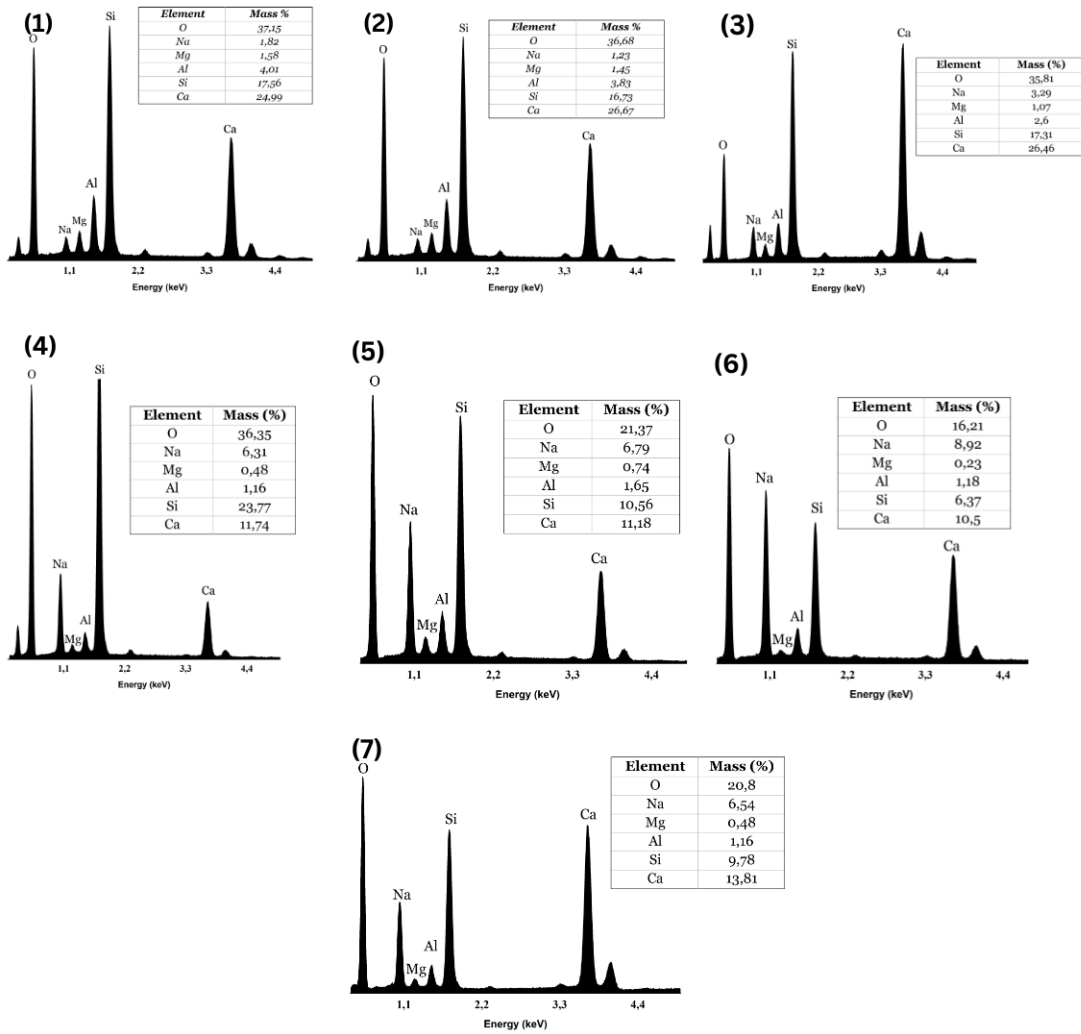


Figure 15 EDX spectra of geopolymers mortars

## 4. Conclusions

Heat-treated recycled fines (HT-RFs) from mortar are used in slag-based geopolymers in this study. Based on study objectives, these conclusions are drawn:

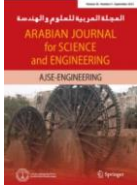
- The addition of HT-RFs to slag-based geopolymer mortars significantly improved their mechanical properties. M30CF had 30.67% higher compressive and 27.31% higher flexural strengths than the reference mortar.
- HT-RFs reduce water-accessible porosity and maintain density, suggesting improved geopolymer mortar durability.
- DIC was combined with other analytical methods to analyze the load-displacement response and identify mortar failure modes. The load-displacement results and ductility indicator trends show that thermal treatment of RFs improves fracture energy absorption and deformation capacity due to powder reactivity and microstructure.
- Thermogravimetric analysis revealed that autoclaved specimens consumed calcium hydroxide (C-H) and formed secondary hydrates. Quantitative analysis showed that P30CF had more C-S-H than P30C. This suggests that the heat-treated recycled fines and liberated calcium hydroxide pozzolanic reaction formed more C-S-H.
- Phase characterization through XRD patterns indicates limited RF participation in geopolymerization due to incomplete C-S-H dissolution. Heat treatment creates highly reactive fines that easily integrate into the aluminosilicate gel network, as shown by increased amorphous hump intensity and crystalline peaks. This supports the increased mechanical performance and reactivity of thermal activation as a cementitious material supplement.
- Mercury intrusion porosimetry shows that tailored thermal activation uniformly incorporates recycled concrete fines into the condensed geopolymer nanostructure, replicating the control paste's pore refinement and mechanical improvements.
- SEM/EDX analysis shows that thermal treatment of RFs in geopolymer mortars improves microstructural cohesion, making materials denser and stronger. These findings suggest that RF heat-treatment can improve geopolymer composite performance.

Optimizing heat treatment parameters, studying long-term durability, and studying geopolymer materials' other properties can help implement and spread these sustainable materials in construction. Overall, this research shows that HT-RFs improve geopolymer mortar performance, promoting greener and more sustainable construction.

## CRedit authorship contribution statement

**Amirouche BERKOUCHE:** Methodology, Formal analysis, Investigation, Data curation, Writing – original draft, Writing – review & editing, Conceptualization, Software, Visualization. **Ahmed Abderraouf BELKADI:** Conceptualization, Methodology, Investigation, Writing – review & editing, Validation, Supervision, Resources, Project administration, Funding acquisition. **Abdelaziz HASNAOUI:** Investigation, Resources, Formal analysis, Software. **Salima Aggoun:** Writing – review & editing, Supervision, Validation. **Tarek Chiker:** Supervision, Formal analysis, Validation. **Abdelhak KHECHAI:** Supervision, Validation, Writing – review & editing. **Annelise COUSTURE:** Investigation, Resources, Formal analysis. **Tayebi TAHAR:** Supervision, Writing – review & editing





## Declaration of competing interest

The authors assert that they have no identifiable financial conflicts of interest or personal affiliations that might have impacted the research presented in this paper.

## Data availability

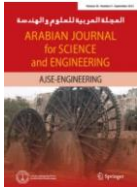
Upon request, data will be provided.

## Acknowledgements

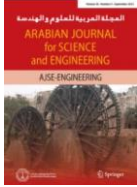
The authors would like to express their gratitude to the Civil Engineering Laboratory at the University of Bordj Bou Arreridj for facilitating the experimental work in this study, as well as to the 'Microscopies & Analyses' imaging center, I-Mat Federation (FR4122) at CY Cergy Paris University (France) for conducting the SEM-EDX analyses.

## References

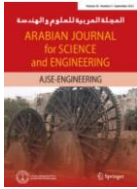
- [1] W. Zuo *et al.*, "Behavior of wire arc additively manufactured 316L austenitic stainless steel single shear bolted connections," *Thin-Walled Structures*, vol. 202, p. 112075, 2024, doi: <https://doi.org/10.1016/j.tws.2024.112075>.
- [2] M.-T. Chen, W. Zuo, Y. Chen, O. Zhao, B. Cheng, and J. Zhao, "Parametric topology optimization design and analysis of additively manufactured joints in spatial grid structures," *Eng Struct*, vol. 300, p. 117123, 2024, doi: <https://doi.org/10.1016/j.engstruct.2023.117123>.
- [3] W. Zuo, M.-T. Chen, Y. Chen, O. Zhao, B. Cheng, and J. Zhao, "Additive manufacturing oriented parametric topology optimization design and numerical analysis of steel joints in gridshell structures," *Thin-Walled Structures*, vol. 188, p. 110817, 2023, doi: <https://doi.org/10.1016/j.tws.2023.110817>.
- [4] G. Bumanis, L. Vitola, I. Pundiene, M. Sinka, and D. Bajare, "Gypsum, geopolymers, and starch-alternative binders for bio-based building materials: A review and life-cycle assessment," *Sustainability (Switzerland)*, vol. 12, no. 14, Jul. 2020, doi: 10.3390/su12145666.
- [5] S. Nenadović *et al.*, "Structural, Mechanical and Chemical Properties of Low Content Carbon Geopolymer," *Sustainability (Switzerland)*, vol. 14, no. 9, May 2022, doi: 10.3390/su14094885.
- [6] Marco Valente, Matteo Sambucci, and Abbas Sibai, "Geopolymers vs. Cement Matrix Materials: How Nanofiller Can Help a Sustainability Approach for Smart Construction Applications—A Review," *Nanomaterials (Basel)*, Aug. 2021.
- [7] N. Kozhukhova, M. Kozhukhova, A. Teslya, and I. Nikulin, "The Effect of Different Modifying Methods on Physical, Mechanical and Thermal Performance of Cellular Geopolymers as Thermal Insulation Materials for Building Structures," *Buildings*, vol. 12, no. 2, Feb. 2022, doi: 10.3390/buildings12020241.



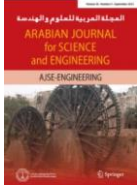
- [8] M. Sarıdemir and S. Çelikten, "Effects of Ms modulus, Na concentration and fly ash content on properties of vapour-cured geopolymer mortars exposed to high temperatures," *Constr Build Mater*, vol. 363, p. 129868, 2023, doi: <https://doi.org/10.1016/j.conbuildmat.2022.129868>.
- [9] M. Sarıdemir and S. Çelikten, "Effect of high temperature, acid and sulfate on properties of alkali-activated lightweight aggregate concretes," *Constr Build Mater*, vol. 317, p. 125886, 2022, doi: <https://doi.org/10.1016/j.conbuildmat.2021.125886>.
- [10] S. Çelikten, "The influence of blast furnace slag content on the mechanical and durability properties of raw perlite-based geopolymer mortars," *Journal of Engineering Research (Kuwait)*, vol. 9, 2021, doi: 10.36909/JER.11225.
- [11] B. Figiela and K. Korniejeno, "The possibility of using waste materials as raw materials for the production of geopolymers," *Acta Innovations*, no. 36, pp. 48–56, Sep. 2020, doi: 10.32933/ActaInnovations.36.4.
- [12] D. Neeraj Varma and S. Prasad Singh, "Recycled waste glass as precursor for synthesis of slag-based geopolymer," *Mater Today Proc*, 2023, doi: 10.1016/j.matpr.2023.03.516.
- [13] A. A. Belkadi *et al.*, "Full Factorial Design of Mechanical and Physical Properties of Eco-mortars Containing Waste Marble Powder," *Arab J Sci Eng*, vol. 48, no. 4, pp. 4325–4338, 2023, doi: 10.1007/s13369-022-06971-7.
- [14] C. L. Wong, K. H. Mo, U. J. Alengaram, and S. P. Yap, "Mechanical strength and permeation properties of high calcium fly ash-based geopolymer containing recycled brick powder," *Journal of Building Engineering*, vol. 32, Nov. 2020, doi: 10.1016/j.jobbe.2020.101655.
- [15] O. Mahmoodi, H. Siad, M. Lachemi, S. Dadsetan, and M. Sahmaran, "Development of ceramic tile waste geopolymer binders based on pre-targeted chemical ratios and ambient curing," *Constr Build Mater*, vol. 258, Oct. 2020, doi: 10.1016/j.conbuildmat.2020.120297.
- [16] C. P. Ganga, J. M. C. Ongpeng, and M. K. M. Daly, "Circular economy on construction and demolition waste: A literature review on material recovery and production," Jul. 01, 2020, *MDPI AG*. doi: 10.3390/ma13132970.
- [17] V. Sata and P. Chindapasirt, "19 - Use of construction and demolition waste (CDW) for alkali-activated or geopolymer concrete," in *Advances in Construction and Demolition Waste Recycling*, F. Pacheco-Torgal, Y. Ding, F. Colangelo, R. Tuladhar, and A. Koutamanis, Eds., in Woodhead Publishing Series in Civil and Structural Engineering. , Woodhead Publishing, 2020, pp. 385–403. doi: <https://doi.org/10.1016/B978-0-12-819055-5.00019-X>.
- [18] R. Shrivastava, B. R. Paramkusam, and S. B. Dwivedi, "Strength and durability performance of geopolymer binder of ambient cured alkali-activated MSW rejected waste and GGBFS mixes," *Environmental Science and Pollution Research*, vol. 29, no. 20, pp. 30521–30536, 2022, doi: 10.1007/s11356-021-17547-7.
- [19] A. Abderraouf Belkadi *et al.*, "Experimental investigation into the potential of recycled concrete and waste glass powders for improving the sustainability and performance of cement mortars properties," *Sustainable Energy Technologies and Assessments*, vol. 64, p. 103710, 2024, doi: <https://doi.org/10.1016/j.seta.2024.103710>.



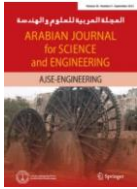
- [20] J. Tan, J. Cai, X. Li, J. Pan, and J. Li, "Development of eco-friendly geopolymers with ground mixed recycled aggregates and slag," *J Clean Prod*, vol. 256, p. 120369, 2020, doi: <https://doi.org/10.1016/j.jclepro.2020.120369>.
- [21] M. Saba and J. J. Assaad, "Effect of recycled fine aggregates on performance of geopolymer masonry mortars," *Constr Build Mater*, vol. 279, Apr. 2021, doi: [10.1016/j.conbuildmat.2021.122461](https://doi.org/10.1016/j.conbuildmat.2021.122461).
- [22] M. Alhawat, A. Ashour, G. Yildirim, A. Aldemir, and M. Sahmaran, "Properties of geopolymers sourced from construction and demolition waste: A review," *Journal of Building Engineering*, vol. 50, p. 104104, 2022, doi: <https://doi.org/10.1016/j.jobe.2022.104104>.
- [23] M. Liu, R. Hu, Y. Zhang, C. Wang, and Z. Ma, "Effect of ground concrete waste as green binder on the micro-macro properties of eco-friendly metakaolin-based geopolymer mortar," *Journal of Building Engineering*, vol. 68, p. 106191, 2023, doi: <https://doi.org/10.1016/j.jobe.2023.106191>.
- [24] D. Zhang, S. Zhang, B. Huang, Q. Yang, and J. Li, "Comparison of mechanical, chemical, and thermal activation methods on the utilisation of recycled concrete powder from construction and demolition waste," *Journal of Building Engineering*, vol. 61, p. 105295, 2022, doi: <https://doi.org/10.1016/j.jobe.2022.105295>.
- [25] H.-J. Ho *et al.*, "Potential investigation of concrete fines as an alternative material: A novel neutralizer for acid mine drainage treatment," *Environ Technol Innov*, vol. 29, p. 102985, 2023, doi: <https://doi.org/10.1016/j.eti.2022.102985>.
- [26] Y. Sui, C. Ou, S. Liu, J. Zhang, and Q. Tian, "Study on properties of waste concrete powder by thermal treatment and application in mortar," *Applied Sciences (Switzerland)*, vol. 10, no. 3, Feb. 2020, doi: [10.3390/app10030998](https://doi.org/10.3390/app10030998).
- [27] K. T. J. Jacques, W. Zengyao, W. Shoude, H. Shifeng, and C. Xin, "The influence of different fine aggregate and cooling regimes on the engineering properties of sulphoaluminate cement mortar after heating," *Case Studies in Construction Materials*, vol. 18, p. e01866, 2023, doi: <https://doi.org/10.1016/j.cscm.2023.e01866>.
- [28] A. Sedaghatdoost and K. Behfarnia, "Mechanical properties of Portland cement mortar containing multi-walled carbon nanotubes at elevated temperatures," *Constr Build Mater*, vol. 176, pp. 482–489, 2018, doi: <https://doi.org/10.1016/j.conbuildmat.2018.05.095>.
- [29] Z. Shui, D. Xuan, W. Chen, R. Yu, and R. Zhang, "Cementitious characteristics of hydrated cement paste subjected to various dehydration temperatures," *Constr Build Mater*, vol. 23, no. 1, pp. 531–537, 2009, doi: <https://doi.org/10.1016/j.conbuildmat.2007.10.016>.
- [30] S. Real, A. Carriço, J. A. Bogas, and M. Guedes, "Influence of the Treatment Temperature on the Microstructure and Hydration Behavior of Thermoactivated Recycled Cement," *Materials*, vol. 13, no. 18, 2020, doi: [10.3390/ma13183937](https://doi.org/10.3390/ma13183937).
- [31] K. Kalinowska-Wichrowska, M. Kosior-Kazberuk, and E. Pawluczuk, "The Properties of Composites with Recycled Cement Mortar Used as a Supplementary Cementitious Material," *Materials*, vol. 13, no. 1, 2020, doi: [10.3390/ma13010064](https://doi.org/10.3390/ma13010064).



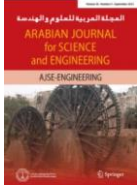
- [32] R. Serpell and F. Zunino, "Recycling of hydrated cement pastes by synthesis of  $\alpha'$ -H-C2S," *Cem Concr Res*, vol. 100, pp. 398–412, 2017, doi: <https://doi.org/10.1016/j.cemconres.2017.08.001>.
- [33] M. F. Funari, S. Spadea, P. Lonetti, and P. B. Lourenço, "On the elastic and mixed-mode fracture properties of PVC foam," *Theoretical and Applied Fracture Mechanics*, vol. 112, p. 102924, 2021.
- [34] S. Real, A. Carriço, J. A. Bogas, and M. Guedes, "Influence of the Treatment Temperature on the Microstructure and Hydration Behavior of Thermoactivated Recycled Cement," *Materials*, vol. 13, no. 18, 2020, doi: 10.3390/ma13183937.
- [35] H. Wu, J. Xu, D. Yang, and Z. Ma, "Utilizing thermal activation treatment to improve the properties of waste cementitious powder and its newmade cementitious materials," *J Clean Prod*, vol. 322, Nov. 2021, doi: 10.1016/j.jclepro.2021.129074.
- [36] S. A. Bernal *et al.*, "Gel nanostructure in alkali-activated binders based on slag and fly ash, and effects of accelerated carbonation," *Cem Concr Res*, vol. 53, pp. 127–144, 2013, doi: <https://doi.org/10.1016/j.cemconres.2013.06.007>.
- [37] A. Cristina, E. Reyes, and A. Moragues, "Ultrafine portland cement performance," *Materiales de Construcción*, vol. 68, p. 157, Jul. 2018, doi: 10.3989/mc.2018.03317.
- [38] A. S. Benosman, H. Taïbi, M. Mouli, Y. Senhadji, and I. Bahlouli, "Destructive and Non-Destructive Tests of PET-Mortar Composites: Characterization by TG/dTG Analysis," 2016.
- [39] "EN-196-1. Methods of testing cement-Part 1: Determination of strength. Quality and Standards Authority of Ethiopia, ES. (2005) 1176-1."
- [40] A. B. D. N. Técnicas, "NBR 9778: Argamassa e concreto endurecidos–Determinação da absorção de água, índices de vazios e massa específica," *Rio de Janeiro*, 2005.
- [41] J. Ibáñez-Gosálvez, T. Real-Herraiz, and J. M. Ortega, "Microstructure, Durability and Mechanical Properties of Mortars Prepared Using Ternary Binders with Addition of Slag, Fly Ash and Limestone," *Applied Sciences*, vol. 11, no. 14, 2021, doi: 10.3390/app11146388.
- [42] A. Ahmad, "Utilizing DIC Technique for Visualizing the Failure Modes of Concrete Specimens," *Civil Engineering Research Journal*, vol. 10, no. 2, Jul. 2020, doi: 10.19080/cerj.2020.10.555783.
- [43] C. Butean and B. Heghes, "Flexure behavior of a hybrid reinforced concrete beam. Strain correlation between mechanical gauges and optical measurement," *Procedia Manuf*, vol. 22, pp. 233–240, Jul. 2018, doi: 10.1016/j.promfg.2018.03.036.
- [44] J. Tan, J. Cai, X. Li, J. Pan, and J. Li, "Development of eco-friendly geopolymers with ground mixed recycled aggregates and slag," *J Clean Prod*, vol. 256, p. 120369, 2020, doi: <https://doi.org/10.1016/j.jclepro.2020.120369>.
- [45] W. Song, J. Yi, H. Wu, X. He, Q. Song, and J. Yin, "Effect of carbon fiber on mechanical properties and dimensional stability of concrete incorporated with granulated-blast furnace slag," *J Clean Prod*, vol. 238, p. 117819, 2019, doi: <https://doi.org/10.1016/j.jclepro.2019.117819>.



- [46] V. W. Y. Tam, M. Soomro, and A. C. J. Evangelista, "Quality improvement of recycled concrete aggregate by removal of residual mortar: A comprehensive review of approaches adopted," *Constr Build Mater*, vol. 288, p. 123066, 2021, doi: <https://doi.org/10.1016/j.conbuildmat.2021.123066>.
- [47] R. Dabbebi, J. L. Barroso de Aguiar, A. Camões, B. Samet, and S. Baklouti, "Effect of the calcinations temperatures of phosphate washing waste on the structural and mechanical properties of geopolymeric mortar," *Constr Build Mater*, vol. 185, pp. 489–498, 2018, doi: <https://doi.org/10.1016/j.conbuildmat.2018.07.045>.
- [48] M. J. Sánchez-Herrero, A. Fernández-Jiménez, Á. Palomo, and L. Klein, "Alkaline Hydration of C2S and C3S," *Journal of the American Ceramic Society*, vol. 99, no. 2, pp. 604–611, Feb. 2016, doi: [10.1111/jace.13985](https://doi.org/10.1111/jace.13985).
- [49] Z. Mirghiasi, F. Bakhtiari, E. Darezereshki, and E. Esmaeilzadeh, "Preparation and characterization of CaO nanoparticles from Ca(OH)<sub>2</sub> by direct thermal decomposition method," *Journal of Industrial and Engineering Chemistry*, vol. 20, no. 1, pp. 113–117, 2014, doi: <https://doi.org/10.1016/j.jiec.2013.04.018>.
- [50] B. Yuan, H. Wang, D. Jin, and W. Chen, "C-S-H Seeds Accelerate Early Age Hydration of Carbonate-Activated Slag and the Underlying Mechanism," *Materials*, vol. 16, no. 4, 2023, doi: [10.3390/ma16041394](https://doi.org/10.3390/ma16041394).
- [51] B. Zhang *et al.*, "Effects of pretreated recycled powder substitution on mechanical properties and microstructures of alkali-activated cement," *Constr Build Mater*, vol. 406, p. 133360, 2023, doi: <https://doi.org/10.1016/j.conbuildmat.2023.133360>.
- [52] E. M. Foley, J. J. Kim, and M. M. Reda Taha, "Synthesis and nano-mechanical characterization of calcium-silicate-hydrate (C-S-H) made with 1.5 CaO/SiO<sub>2</sub> mixture," *Cem Concr Res*, vol. 42, no. 9, pp. 1225–1232, 2012, doi: <https://doi.org/10.1016/j.cemconres.2012.05.014>.
- [53] Q. Gao, Z. Ma, J. Xiao, and F. Li, "Effects of Imposed Damage on the Capillary Water Absorption of Recycled Aggregate Concrete," *Advances in Materials Science and Engineering*, vol. 2018, 2018, doi: [10.1155/2018/2890931](https://doi.org/10.1155/2018/2890931).
- [54] O. Mohamed, E. Ahmed, O. Najm, K. Al-Arife, and E. Hijah, "Water absorption characteristics and rate of strength development of mortar with slag-based alkali-activated binder and 25% fly ash replacement," *Mater Today Proc*, 2023, doi: <https://doi.org/10.1016/j.matpr.2023.02.411>.
- [55] N. H. Jamil, Mohd. M. A. B. Abdullah, F. Che Pa, H. Mohamad, W. M. A. W. Ibrahim, and J. Chaiprapa, "Influences of SiO<sub>2</sub>, Al<sub>2</sub>O<sub>3</sub>, CaO and MgO in phase transformation of sintered kaolin-ground granulated blast furnace slag geopolymer," *Journal of Materials Research and Technology*, vol. 9, no. 6, pp. 14922–14932, 2020, doi: <https://doi.org/10.1016/j.jmrt.2020.10.045>.
- [56] Z. L. Xie, H. F. Zhou, L. J. Lu, and Z. A. Chen, "An investigation into fracture behavior of geopolymer concrete with digital image correlation technique," *Constr Build Mater*, vol. 155, pp. 371–380, 2017, doi: <https://doi.org/10.1016/j.conbuildmat.2017.08.041>.



- [57] H. Chang, X. Yan, W. Zuo, J. Xia, and T. Yu, "Numerical analysis and design methods of grout-filled GFRP tube repaired corroded CHS T-joints," *Thin-Walled Structures*, vol. 198, p. 111719, 2024, doi: <https://doi.org/10.1016/j.tws.2024.111719>.
- [58] W. Zuo, M.-T. Chen, and B. Young, "Structural behaviour of cold-formed steel elliptical hollow section stub columns after exposure to ISO-834 fire curve," *Thin-Walled Structures*, vol. 197, p. 111309, 2024, doi: <https://doi.org/10.1016/j.tws.2023.111309>.
- [59] P. K. Sarker, R. Haque, and K. V Ramgolam, "Fracture behaviour of heat cured fly ash based geopolymer concrete," *Mater Des*, vol. 44, pp. 580–586, 2013, doi: <https://doi.org/10.1016/j.matdes.2012.08.005>.
- [60] M. Ben Haha, G. Le Saout, F. Winnefeld, and B. Lothenbach, "Influence of activator type on hydration kinetics, hydrate assemblage and microstructural development of alkali activated blast-furnace slags," *Cem Concr Res*, vol. 41, no. 3, pp. 301–310, 2011, doi: <https://doi.org/10.1016/j.cemconres.2010.11.016>.
- [61] I. Nikolić, L. Karanović, I. J. Častvan, V. Radmilović, S. Mentus, and V. Radmilović, "Improved compressive strength of alkali activated slag upon heating," *Mater Lett*, vol. 133, pp. 251–254, 2014, doi: <https://doi.org/10.1016/j.matlet.2014.07.021>.
- [62] A. A. Belkadi, S. Aggoun, C. Amouri, A. Geuttala, and H. Houari, "Effect of vegetable and synthetic fibers on mechanical performance and durability of Metakaolin-based mortars," *J Adhes Sci Technol*, vol. 32, no. 15, pp. 1670–1686, Aug. 2018, doi: [10.1080/01694243.2018.1442647](https://doi.org/10.1080/01694243.2018.1442647).
- [63] D. Bravo Hidalgo, O. Kessal, A. Bennia, A. Belkadi, and M. L. Khouadjia, "Experimental investigation of High-Performance Concrete subjected to high temperatures," *Revista Ingeniería de Construcción*, vol. 38, Apr. 2023, doi: [10.7764/RIC.00056.21](https://doi.org/10.7764/RIC.00056.21).
- [64] A. A. Belkadi, O. Kessal, S. Bensalem, S. Aggoun, C. Amouri, and M. L. K. Khouadjia, "Aggregate Type Influence on Microstructural Behavior of Concrete Exposed to Elevated Temperature," *Civil and Environmental Engineering Reports*, vol. 32, no. 1, pp. 19–42, 3922, doi: [doi:10.2478/ceer-2022-0002](https://doi.org/10.2478/ceer-2022-0002).
- [65] I. Amer, M. Kohail, M. S. El-Feky, A. Rashad, and M. A. Khalaf, "A review on alkali-activated slag concrete," *Ain Shams Engineering Journal*, vol. 12, no. 2, pp. 1475–1499, 2021, doi: <https://doi.org/10.1016/j.asej.2020.12.003>.
- [66] J. L. Provis, G. C. Lukey, and J. S. J. van Deventer, "Do Geopolymers Actually Contain Nanocrystalline Zeolites? A Reexamination of Existing Results," *Chemistry of Materials*, vol. 17, no. 12, pp. 3075–3085, 2005, doi: [10.1021/cm050230i](https://doi.org/10.1021/cm050230i).
- [67] X. Wan, H. Li, X. Che, P. Xu, C. Li, and Q. Yu, "A Study on the Application of Recycled Concrete Powder in an Alkali-Activated Cementitious System," *Processes*, vol. 11, no. 1, 2023, doi: [10.3390/pr11010203](https://doi.org/10.3390/pr11010203).
- [68] L. Reig, M. M. Tashima, M. V Borrachero, J. Monzó, C. R. Cheeseman, and J. Payá, "Properties and microstructure of alkali-activated red clay brick waste," *Constr Build Mater*, vol. 43, pp. 98–106, 2013, doi: <https://doi.org/10.1016/j.conbuildmat.2013.01.031>.



- [69] J. Li, X. Dang, J. Zhang, P. Yi, and Y. Li, "Mechanical Properties of Fly Ash-Slag Based Geopolymer for Repair of Road Subgrade Diseases," *Polymers (Basel)*, vol. 15, no. 2, 2023, doi: 10.3390/polym15020309.
- [70] J. Xu, A. H. Kang, Z. G. Wu, P. Xiao, B. Li, and Y. M. Lu, "Research on the Formulation and Properties of a High-Performance Geopolymer Grouting Material Based on Slag and Fly Ash," *KSCE Journal of Civil Engineering*, vol. 25, no. 9, pp. 3437–3447, 2021, doi: 10.1007/s12205-021-1699-9.